ADVANCED FUNCTIONAL MATERIALS
www.afm-journal.de

Modulating Two-Photon Absorption in a Pyrene-Based MOF Series: An In-Depth Investigation of Structure–Property Relationships

Simon N. Deger, Helmy Pacheco Hernandez, Yang Cui, Hongxing Hao, Vanessa Ramm, David C. Mayer, Khai-Nghi Truong, Roland A. Fischer, Jürgen Hauer, Mariana Kozlowska,* and Alexander Pöthig**

Metal–organic frameworks (MOFs) are emerging as promising materials for multiphoton absorption (MPA), a nonlinear optical phenomenon relevant for applications, such as bioimaging, phototherapy, and photonic devices. However, the structural features that govern their exceptional MPA activity remain poorly understood. To address this, a family of pyrene-based MOFs (NU-1000, NU-901, SrTBAPy, and BaTBAPy), that vary in topology and secondary building units (SBUs), is systematically investigated. Significant differences are observed in the two-photon absorption (2PA) cross-section $\sigma^{(2)}$, with BaTBAPy exhibiting the highest activity (8.2×10^4 GM). Quantum mechanical calculations reveal that intermolecular chromophore interactions and SBU-induced effects contribute strongly to enhanced $\sigma^{(2)}$ values, particularly in NU-901 and BaTBAPy. The findings demonstrate that both framework topology and metal coordination environments are critical to modulating MPA behavior. These insights into the structure–property relationships of MOFs pave the way for rational design of next-generation nonlinear optical materials.

1. Introduction

Optical nonlinearities in photoactive materials arise from their interaction with intense laser fields, leading to a wide range of phenomena that form the foundation of nonlinear optics (NLO).[1] One of these phenomena is multiphoton absorption (MPA), which has garnered significant attention in recent years due to its pivotal role in diverse applications.[2] Many of today's advanced technologies are applying MPA. These include key areas such as biomedical imaging (deep tissue imaging and fluorescence microscopy),[3] medical applications (photodynamic therapy),[4] materials science (3D microfabrication),[5] and photonics (optical limiting).[6]

Given the diverse range of interdisciplinary applications, extensive research has been conducted to explore the MPA properties of various material classes.[2a] These include inorganic materials, such as nanocrystals, quantum dots, nanowires, perovskites, metal clusters, and organic materials like chromophores, dendrimers, and polymers.[2a,7] Recently, the focus has shifted toward hybrid materials, particularly coordination polymers (CPs) and their porous subclass, metal–organic frameworks (MOFs).[8] MOFs offer unique advantages, including the ability to control aggregation effects and enhance the stability of chromophores.[9] This is achieved by introducing coordinating groups, such as carboxylic

S. N. Deger, V. Ramm, D. C. Mayer, R. A. Fischer, A. Pöthig
Technical University of Munich
TUM School of Natural Sciences
Department of Chemistry
Chair of Inorganic and Metal–Organic Chemistry
Catalysis Research Center
85747 Garching, Germany
E-mail: alexander.poethig@tum.de

The ORCID identification number(s) for the author(s) of this article can be found under https://doi.org/10.1002/adfm.202506660

DOI: 10.1002/adfm.202506660

H. Pacheco Hernandez, M. Kozlowska
Institute of Nanotechnology (INT)
Karlsruhe Institute of Technology (KIT)
Kaiserstr. 12, 76131 Karlsruhe, Germany
E-mail: mariana.kozlowska@kit.edu

Y. Cui, H. Hao, J. Hauer
Technical University of Munich
TUM School of Natural Sciences
Department of Chemistry
Professorship for Dynamic Spectroscopy
Catalysis Research Center
85747 Garching, Germany
E-mail: juergen.hauer@tum.de

K.-N. Truong
Rigaku Europe SE
Hugenottenallee 167, 63263 Neu-Isenburg, Germany

acids, to chromophores that bind to secondary building units (SBUs), typically metal-oxo clusters. These serve as nodes connecting organic linkers in the MOF structure, thereby fixing the chromophores in a stable solid-state structure.[10]

The modular structure of MOFs, governed by the principles of reticular chemistry, serves as a robust framework for investigating the key factors influencing MPA and enables the systematic design of chromophore arrangements to elucidate direct structure–property relationships.[8b] Therefore, several linkers, SBUs, and corresponding CPs and MOFs have been investigated for their MPA activity.[8b] Notably, anthracene, carbazole-, and aggregation-induced emission dyes based on tetra(4-carboxylphenyl)ethylene, which exhibited the highest two-photon absorption (2PA) activity (up to 7.4×10^7 GM) in a dense Zn-MOF, have been incorporated into frameworks.[11] Here, GM abbreviates the unit Göppert–Mayer, 1 GM = 10^{-50} cm^4 s Photon^{-1} molecule^{-1}. However, studies aiming to identify structure–property relationships have proven challenging due to the numerous factors that influence and alter the observed activity.[8b,11c]

To date, several factors have been identified to contribute to the enhancement of the 2PA cross-section $\sigma^{(2)}$ of chromophores in MOFs.[8b] These are the rigidity of the linker enforced by the framework, reducing radiation-less decay pathways, polarization by the SBU, and intermolecular interactions between the packed chromophores.[11b,c,e] However, especially intermolecular interactions and the interplay between the contributing factors remain poorly understood due to the intricate relationships among them and the inherent complexity of the materials, posing challenges for drawing direct conclusions and providing definitive insights.[8b,11l]

In this study, we present our efforts toward this by investigating the polymorphic structures of NU-1000 and NU-901 for their 2PA-activity. They are possessing the same stoichiometry, with the linker 1,3,6,8-tetrakis(*p*-benzoic acid)pyrene (H_4TBAPy) and a zirconium oxo-cluster as the SBU. They hold differing ligand orientations, making the direct observation of structure–property relationships possible. Additionally, we selected two other MOFs, SrTBAPy and BaTBAPy, using the same linker but incorporating different metals (Sr and Ba), resulting in distinct SBU geometries and, thus, differing denser framework topologies and closely packed linker positions. The MPA performance was investigated through a comparative analysis of linker distances within the MOF and the structural influence of the SBUs. To explore the molecular features of $TBAPy^{4-}$ in the frameworks and to investigate why different MOF compositions lead to a change in MPA activity, we conducted time-dependent density functional theory (TD-DFT) calculations followed by in-depth analysis of the electron density changes during light absorption, permitting the quantification of the charge transfer characteristics for electronic transitions. It allowed us to understand the role of the MOFs topology and SBUs under varying stacking arrangements and its impact on the observed MPA increase. The short inter-chromophore distances of BaTBAPy, which allow for stronger electronic coupling, along with the coordination to the SBU that alters electron delocalization within the assemblies, were found to modulate the charge transfer characteristics and enhance $\sigma^{(2)}$ more efficiently than the increased polarization induced by the Sr-based SBUs reported previously.[11f,k]

2. Results and Discussion

2.1. Synthesis and Characterization

For the synthesis of potentially MPA-active MOFs, H_4TBAPy (**Figure 1**) was chosen as the linker due to its extended π-electron system and a polarizable π-core that are promised to trigger a high nonlinear response.[2a,11a,e,i,j,l] It was synthesized in a two-step synthesis starting from 1,3,6,8-tetrabromopyrene, which is converted in a *Suzuki* coupling reaction to Et_4TBAPy. This is subsequently used in the saponification, after which H_4TBAPy is obtained (details can be found in the Supporting Information).[12]

Following the successful synthesis of H_4TBAPy, this linker was employed in the synthesis of NU-1000 and NU-901 (Figure 1).[13] Both feature $Zr_6(\mu_3\text{-}OH)_4(\mu_3\text{-}O)_4(OH)_4(OH_2)_4$ SBUs that form polymorphic structures with H_4TBAPy, which makes the following direct analysis of structure–property relationships regarding MPA possible.

Using biphenyl-4-carboxylic acid as the modulator, pure NU-1000 is obtained, appearing in the *csq* topology (Figure 1).[13a] The linkers form 31 Å hexagonal pores and 11 Å triangular pores in diameter, with the shortest center-to-center distance of 10.94 Å in the triangular pores. Its powder X-ray diffraction (PXRD) pattern matches with the calculated PXRD data obtained from single crystal X-ray diffraction (SC-XRD), and the characteristic (100) reflection at 2.5° is present with high crystallinity (Figure S4, Supporting Information). Nitrogen adsorption measurements unveil a Brunauer–Emmett–Teller (BET) surface of 2023 m^2 g^{-1} and the characteristic mesoporous step (Figure S9, Supporting Information). Scanning electron microscope (SEM) analysis reveals the characteristic rod-shaped hexagonal crystals (Figure S13a, Supporting Information), showing a successful synthesis of NU-1000.

To obtain phase pure NU-901 in the *scu* topology (Figure 1), 4-aminobenzoic acid is employed as the modulator in the synthesis step of the Zr-oxo cluster.[13b] It possesses 11 Å-wide rhomboid-shaped pores, with the shortest center-to-center distances of all linkers of 9.52 Å. The observed PXRD pattern is missing the reflection at 2.5°, proving the absence of NU-1000 side-phase. The comparison with the calculated PXRD pattern from the SC-XRD structure shows good agreement (Figure S5, Supporting Information). Combined with the characteristic BET-area of 1960 m^2 g^{-1} and SEM images showing the characteristic oval crystals (Figure S13b, Supporting Information).Therefore, a successful and phase pure synthesis of NU-901 can be assumed.

In addition to the two polymorphic structures, SrTBAPy was synthesized due the closer distance between linkers as compared to NU-1000 and NU-901 with its *frz* topology (Figure 1).[14] However, due to its differing SBU (Figure 1), the results cannot be as easily compared as in the polymorphic structures and the additional effect of the metal on NLO properties must be included. Therefore, the metal impact was analysed in detail by DFT.[11f,k,15] Following a known procedure in the literature, SrTBAPy was obtained through solvothermal synthesis from $Sr(NO_3)_2$ and H_4TBAPy.[14] The SBU is based on infinite chains of alternating Sr- and O-atoms connecting the carboxylic acid groups of the MOF. The layers are stacked directly on each other, with no offset between the pyrene cores of adjacent layers, and the interlayer spacing measures 6.86 Å (Figure 1). The comparison with the

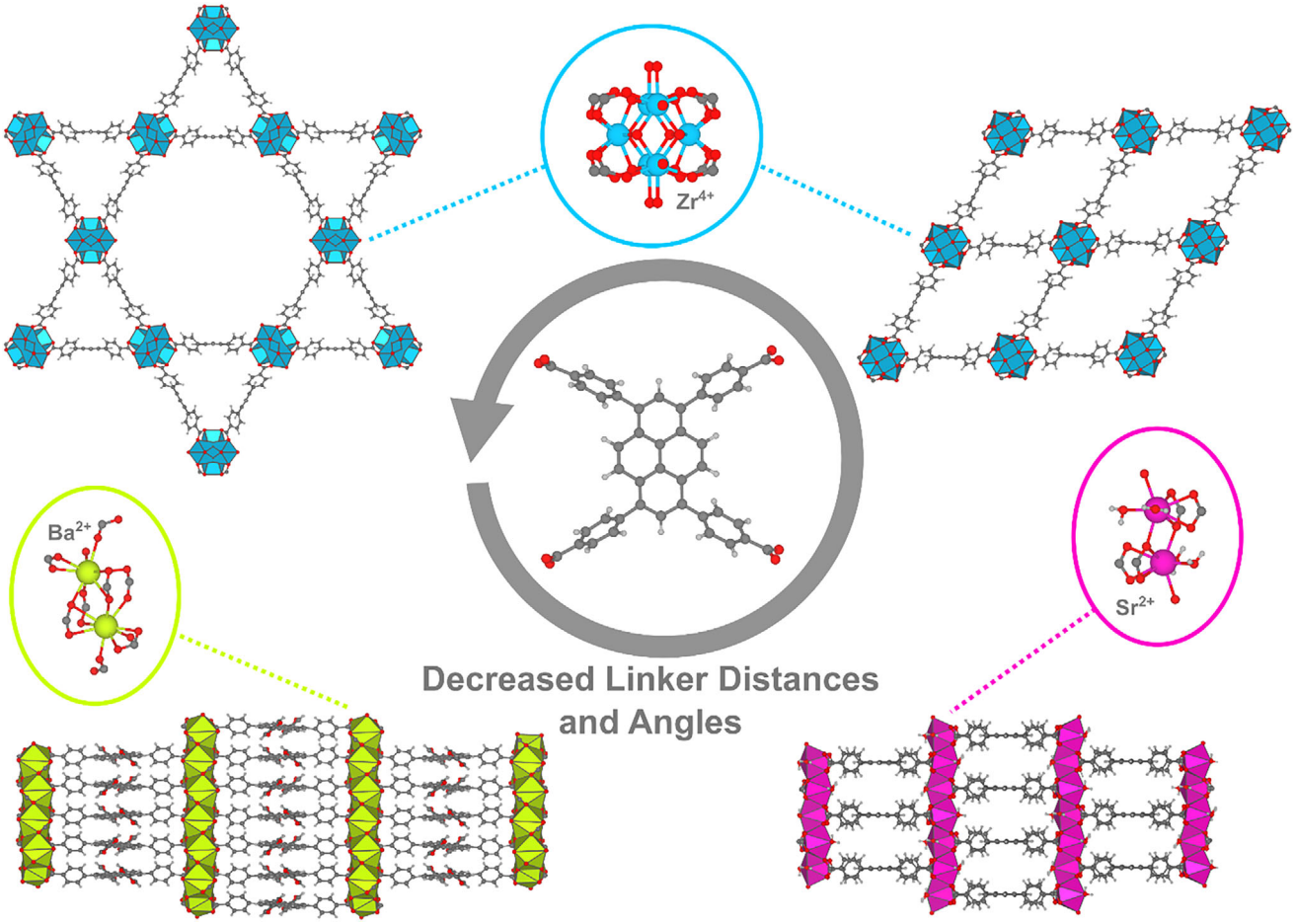

Figure 1. Schematic structures of the linker $TBAPy^{4-}$ (middle), NU-1000 (top left), NU-901 (top right), and their corresponding SBU consisting of a $Zr_6(\mu_3\text{-}OH)_4(\mu_3\text{-}O)_4(OH)_4(OH_2)_4$ cluster (blue), as well as BaTBAPy (bottom left) with the corresponding rod Ba-based SBU (yellow) and SrTBAPy (bottom right) with the corresponding Sr-rod SBU (pink). Color coding: light gray = hydrogen, gray = carbon, blue = zirconium, red = oxygen, yellow = barium, and pink = strontium.

calculated PXRD pattern from the SC-XRD structure also shows good agreement (Figure S6, Supporting Information).

BaTBAPy was synthesized to enable comparison with the previous three MOF structures, featuring an even shorter distance between chromophores within the MOF framework (Figure 1). It is formed through the reaction of $Ba(NO_3)_2$ with H_4TBAPy in DMF at 85 °C with the addition of H_2O and HCl. This synthesis afforded needle-shaped clear yellow single crystals, which were analyzed by continuous rotation 3D electron diffraction (3D ED), PXRD, TGA, and IR, revealing and confirming the composition $[Ba_2TBAPy(DMF)_2] \times (H_2O)_2$, with the same topology as recently reported.[16] 3D ED analysis shows that BaTBAPy crystallizes in the monoclinic space group $C2/c$ with the unit cell parameters $a = 25.10(12)$ Å, $b = 21.56(8)$ Å, $c = 8.11(11)$ Å and $\alpha = 90°$, $\beta = 97.0(2)°$, $\gamma = 90°$. It comprises infinite double strands of Ba connected by O atoms growing along the *c*-axis, functioning as the SBU. Each Ba is coordinated to nine O atoms, one of which stems from a coordinated DMF and the other of the six $TBAPy^{4-}$ units. Each $TBAPy^{4-}$, in turn, is connected to twelve O atoms, forming two different coordination modes. They are either monodentate bridging to three barium ions and bidentate chelating to another barium ion ($\mu^4\text{-}\eta^1\text{:}\eta^2\text{:}\eta^1\text{:}\eta^1$) or both monodentate bridging to one and bidentate chelating to another barium ion ($\mu^2\text{-}\eta^1\text{:}\eta^2$), which are on the opposite two sides of each linker atom in the MOF structure. The arrangement of ligands around the Ba atoms forms a 3D porous network, with channels accessible along the *c*-axis. The $TBAPy^{4-}$ core units are separated by 3.41 Å and are oriented at a 10.17° angle to each other, with a twisted configuration between them (Figure 1). The comparison with the calculated PXRD pattern from the SC-XRD structure also shows good agreement (Figures S7 and S8, Supporting Information).

2.2. Steady State Spectroscopy of H_4TBAPy and MOFs

After successfully synthesizing and characterizing the linker and four MOFs, 1PA optical spectroscopy was performed (**Figure 2**). The absorption spectrum of the linker H_4TBAPy in DMF shows maxima at 304 and 391 nm (Figure 2a).

Considering the *implicit* DMF solvent, time-dependent DFT calculations reproduced the main transitions with the maximum at 277 and 368 nm, respectively, corresponding to the 4th and

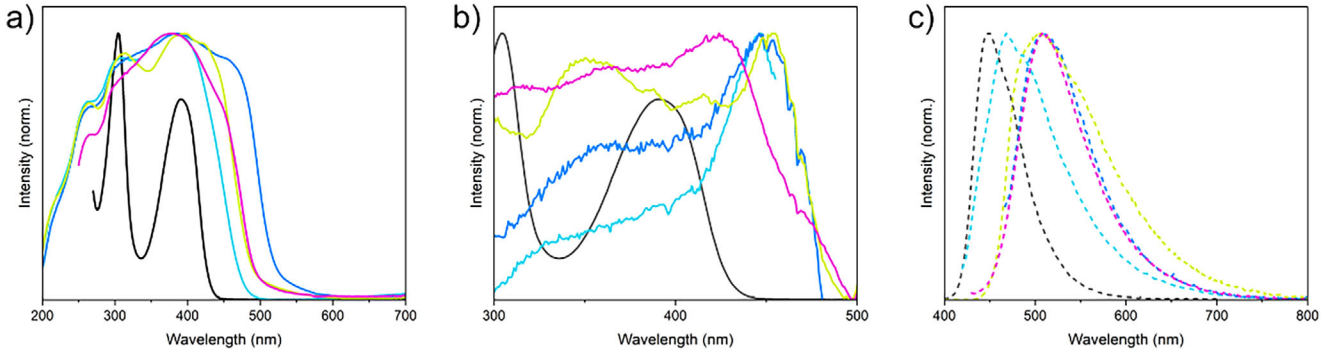

Figure 2. a) UV–vis of H_4TBAPy (black line) and diffuse reflectance spectra of the MOFs (turquoise = NU-1000, blue = NU-901, pink = SrTBAPy, and yellow = BaTBAPy). b) Fluorescence-excitation spectra of the MOFs. c) Emission spectra of the linker and MOFs.

1st excitations. The character of these excitations predominantly involves intramolecular charge-transfer (CT) (Table S6, Supporting Information). Minor spectral shifts within the main spectral bands were observed for the linker extracted from the crystal structure of four MOFs studied (Figures S33–S35, Supporting Information). After careful consideration, it was attributed to slight geometrical changes of the linker within the specific MOF, resulting in close-lying local minima. For consistency, we have considered only the lowest-energy conformer optimized in *implicit* DMF, i.e., originated from NU-901. All four MOFs show broadened diffuse reflectance spectra with a redshift compared to the linker (Figure 2a). In the fluorescence excitation spectra, the redshift is visible in the maxima of the MOFs, which are shifted to 424 nm for SrTBAPy, 446 nm for NU-1000, 447 nm for NU-901, and 454 nm for BaTBAPy (Figure 2b). The shift observed in the calculated spectra of the extracted H_4TBAPy assemblies follows a similar trend to that of the linker spectra extracted from each corresponding MOF (Figures S34 and S35, Supporting Information). Such an observation indicates ground-state interactions between linkers in the MOFs directly impacting the transition orbitals and the electronic transitions' character (Table S6, Supporting Information). The primary transition for the first band (94.4%) occurs between the highest occupied molecular orbital (HOMO) and the lowest unoccupied molecular orbital (LUMO), due to the absence of molecular aggregation. Thus, in the monomer, the transitions are dominated by local excitons and exhibit low intramolecular CT contributions (Table S6, Supporting Information). However, after incorporating the linkers into the MOFs, these orbitals are either delocalized over the whole assembly (e.g., DimerB of NU-1000 (Table S7b, Supporting Information) or NU-901 (Table S8b, Supporting Information)) or additional contribution of transitions between HOMO-1 to LUMO (54%) and HOMO to LUMO+1 (40.6%) localized on different fragments of the dimer appear (Table S8a, Supporting Information). This corresponds to additional intermolecular CT transitions, which are even more pronounced in larger assemblies (e.g., in TrimerB of NU-901, TrimerA of SrTBAPy and BaTBAPy depicted in Table S8d,S9b, and S10b, respectively, Supporting Information). Thus, due to the diverse packing of molecules in the material (Table S5, Supporting Information), the absorption bands, considering a particular assembly unit, are slightly shifted. This is a major contribution to the experimentally observed line broadening.

To assess the impact of Sr- and Ba-based SBUs on the 1PA spectra, calculations were performed on monomers and dimers derived from the MOF, both with and without the SBUs. From Figure S35c and S35d (Supporting Information), it could be deduced that SBUs only negligibly shift the lowest band (by 3–4 nm) to the higher wavelengths with some more pronounced oscillator strength decrease in the case of SrTBAPy. A larger spectral shift is observed for SrTBAPy, as the H_4TBAPy linker geometry in this structure exhibits a more pronounced blueshifted absorption compared to all other cases (Figure S36, Supporting Information). No other significant changes were observed.

The emission spectra of all MOFs show a redshift compared to the monomer spectrum (black and colored dashed lines in Figure 2c). H_4TBAPy has its emission maximum at 450 nm while NU-1000, NU-901, BaTBAPy, and SrTBAPy at 468, 507, 506, and 508 nm, respectively. It indicates that NU-1000 possesses a higher contribution of the monomeric states emission (probably from the linkers forming a larger pore), while other systems are shifted toward the aggregation-like emission. The respective fluorescence quantum yields (QY) in MOFs are lower than those for H_4TBAPy in solution ($\Phi = 76\%$), which can be explained by differing factors, such as the aggregation of chromophores in the MOFs.[11g] Specifically, NU-1000 shows a solid state QY of $\Phi = 12.3\%$, NU-901 of $\Phi = 9.46\%$, SrTBAPy of $\Phi = 31.7\%$, while Φ is 20.4% in BaTBAPy.

2.3. Two-Photon Fourier-Transform Spectroscopy (2P-FTS) Measurements

The 2PA of the MOFs and the linker samples were prepared and analyzed using a previously described method and a 2P-FTS spectrometer.[11g] The excitation spectra span a wavelength range from 720 to 920 nm (**Figure 3**). $\sigma^{(2)}$ values were calibrated using fluorescein in water (pH 11) for the H_4TBAPy linker and $[Zn_{2n}(sbcd)(DMAc)_{2n}(H_2O)_{1.5n}]$ for the MOFs.[11f,17] (Note: The 2PA activity in the MOFs is an average of several points of the prepared PMMA film. We expect that the 2PA is dependent on the orientation of the anisotropic crystals, therefore in addition to the mean values additional maxima and minima of the prepared PMMA films of each MOF are given in Table S4 (Supporting Information). The linker shows a weak $\sigma^{(2)}$ of 9.4 – 0.5 GM in the measured wavelength range (Figure 3a). The calculations of

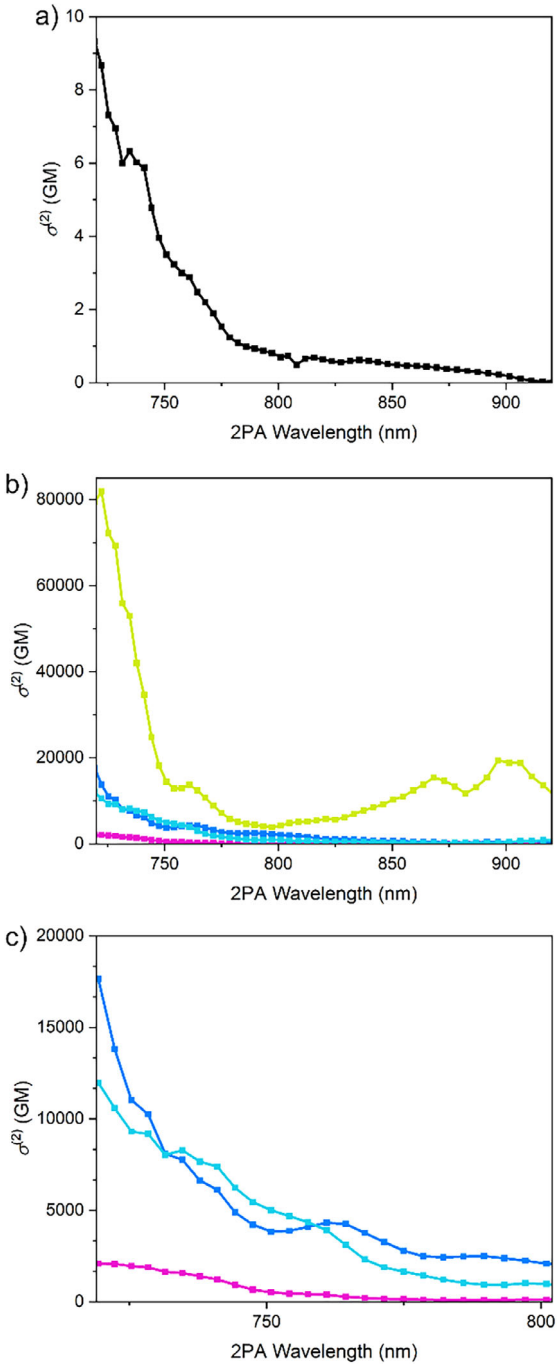

Figure 3. a) Experimental 2PA spectrum of H_4TBAPy in DMF (black dots and line). b) 2PA spectra of NU-1000 (turquoise), NU-901 (blue), SrTBAPy (pink), and BaTBAPy (dark yellow). c) Enlarged 2PA spectra of NU-1000 (turquoise), NU-901 (blue), and SrTBAPy (pink) in the range from 720 to 805 nm.

2PA in the H_4TBAPy monomer showed a low $\sigma^{(2)}$ of 0.007 GM at 737 nm, corresponding to the first excitation. This transition involves predominantly intramolecular CT, as detailed in Table S6 (Supporting Information). However, this is the $\sigma^{(2)}$ value of the geometrically relaxed linker in *implicit* solvent without considering its vibrational flexibility and explicit solvent effects. The rotational flexibility of the phenyl rings of the H_4TBAPy linker is relatively high. Therefore, the 2PA at room temperature conditions may deviate. The variation in the 2PA response as a function of phenyl ring rotations can be illustrated by the exemplary 2PA calculations for the linkers extracted from the studied MOFs, without geometry optimization (Figure S34, Supporting Information). Additionally, it is important to note that direct comparison of the absolute values of the calculated and measured $\sigma^{(2)}$ should be approached with caution, as no rescaling was performed using reference systems, as standard protocols are still unavailable.

After incorporation of the linker into the MOFs, the 2PA activity of all the studied systems gets enhanced. Here, SrTBAPy shows the lowest $\sigma^{(2)}$ of all investigated MOFs, i.e., 2.1×10^3 GM at 719 nm with lowering to 24 GM at 916 nm. This is quite surprising, because previously the MOFs reported with Sr-based SBUs exhibited strong polarization effects, enhancing the $\sigma^{(2)}$.[11a,k] Additionally, SrTBAPy features shorter interchromophore distances (in comparison to NU-1000 and NU-901) with coplanar arrangements previously shown to be favorable.[11a,e]

Both NU-1000 and NU-901 show much higher but comparatively similar activity with $\sigma^{(2)}$: 1.2×10^4 to 1.9×10^3 GM and 1.8×10^4 to 3.4×10^3 GM, respectively. However, the 2PA of BaTBAPy is 4–7 times stronger than NU-1000 and NU-901, resulting in a $\sigma^{(2)}$ of 8.2×10^4 GM at 719 nm to 3.9×10^3 GM at 797 nm (Figure 3b), significantly outperforming SrTBAPy. Contrary to expectations, the 2PA activity in the investigated MOFs follows the order SrTBAPy < NU-1000 < NU-901 < BaTBAPy. Previous studies suggest that denser chromophore packing typically enhances $\sigma^{(2)}$, proposing that factors, such as rigidification and intermolecular CT may play a role.[11a,l] Based on this, the expected trend would have been NU-1000 < NU-901 < SrTBAPy < BaTBAPy, which differs from the observed trend with NU-1000 and NU-901 showing a better 2PA activity than SrTBAPy.[11a,e,f] To investigate the molecular origins of the observed 2PA trends in relation to MOF topology and linker packing, TD-DFT calculations were performed. Specifically, the 2PA spectra of various dimers, trimers, and, when possible, tetramers of the linkers were calculated (Figure S32 and Tables S5,S6, Supporting Information).

The key observations, considering the most 2PA-active assemblies, are summarized in **Figure 4**. NU-1000 shows a threefold increase in $\sigma^{(2)}$ upon trimer formation in the triagonal pore as compared to the dimer-based assembly. This increase is partially attributed to intramolecular CT, as shown in Table S8 (Supporting Information). However, the most contributing factor to the increase of $\sigma^{(2)}$ in this assembly type are excitons formed upon light absorption in the micropores (Table S8e, Supporting Information). NU-1000 was already reported for its exciton confinement in the small triangular pore,[18] which is apparently a driver for the enhancement of $\sigma^{(2)}$ after the incorporation into the MOF. Meanwhile, the contribution from chromophores within the hexagonal pore is negligible (the 2PA spectrum of DimerD in Figure S36a, Supporting Information). This near inactivity in the hexagonal pore, possibly due to larger chromophore distances, limits the positive effect of the triangular pore from spanning the entire material by isolating them in the structure, hindering a greater cumulative effect of the arranged chromophores. As a result, the potential for a greater increase in the 2PA signal within the material is hindered.

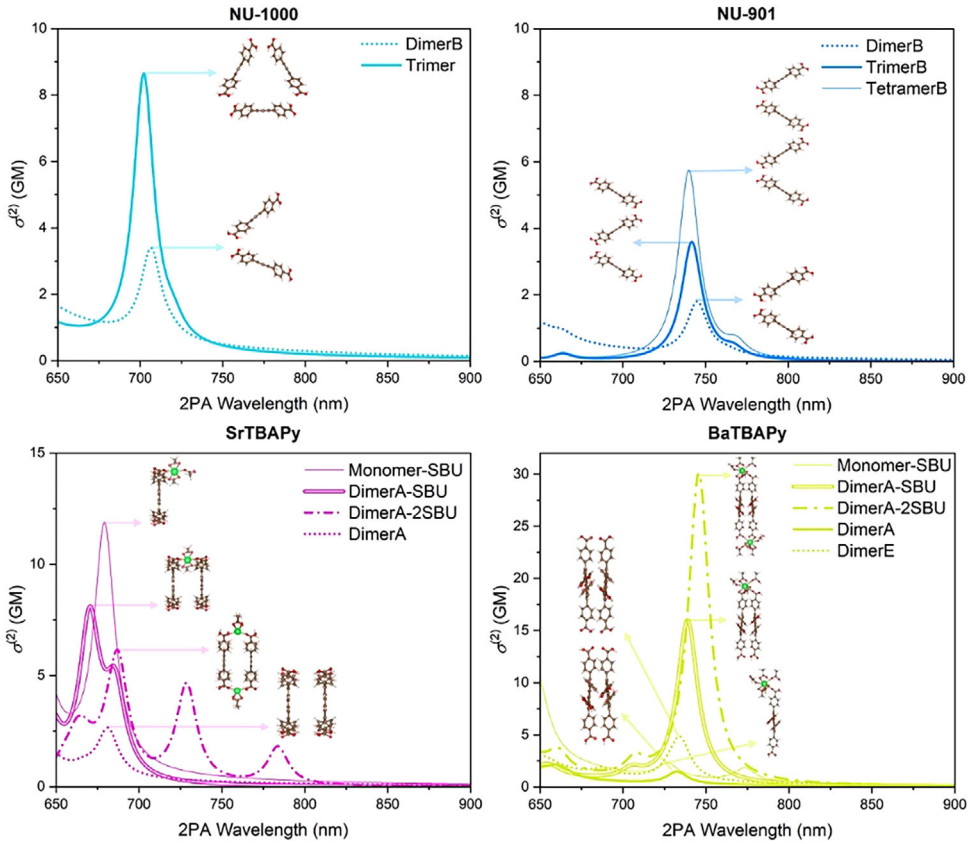

Figure 4. Effect of MOF packing on the 2PA response in the calculated 2PA spectra of assemblies extracted from the crystal structures. The H_4TBAPy monomer was excluded in visualization due to its negligible $\sigma^{(2)}$ in the measured spectral range. More detailed analysis is given in the Supporting Information.

This changes with the MOF topology in NU-901, which allows excitons to travel along an oriented zig-zag direction within the a-b plane, potentially extending throughout the entire material (as shown in the inset of Figure 4b).[18a] Therefore, the exciton hopping occurs according to a different pathway than in NU-1000 and enhances $\sigma^{(2)}$. It can be seen by the visible increase of $\sigma^{(2)}$ from 1.60 GM for DimerB to 3.56 GM in TrimerB and finally to 5.72 GM in the case of TetramerB (Figure 4b). Thus, through-space interactions participate in the enhancement of the 2PA response. TrimerB shows enhanced activity compared to DimerB, which is enabled by local excitons and intra- and intermolecular CT, whereby the intermolecular CT is only present in the trimer. The presence of local excitons, as well as the CT contributing to the observed response was revealed by the electron–hole analysis as explained in the Supporting Information. The addition of a pyrene unit in the same direction (TetramerB) allowed us to check if this enhancement might be sustained in the whole MOF. We see that local excitons mainly dominate the transitions in this tetramer, and in addition, intramolecular CT is present. It is expected that the excitonic interactions along this direction in NU-901 will further grow with each added $TBAPy^{4-}$ unit compared to the self-contained trimers of NU-1000 that are isolated.[11e,18a] This difference arises solely from their distinct topologies, which, in the case of NU-901, allow for an extended network of interacting chromophores. We should note that the analysis of the trimers and tetramers representing the pore environment along three sides of the pore in NU-901 (i.e., TrimerA and TetramerA visualized in Table S5, Supporting Information), indicated no significant enhancement of the 2PA within this pathway: $\sigma^{(2)}$ is 1.03 GM and 1.48 GM, respectively (Figure S36b, Supporting Information). Therefore, it can be observed that the not only the chromophore distance in the MOFs plays a role in modulating $\sigma^{(2)}$, but also the spatial arrangement.[18a] Since TD-DFT calculations were performed for only a few molecules (a maximum of four), disregarding the packing density and the material's volume, the reported $\sigma^{(2)}$ are lower than those shown in Figure 3. Therefore, we primarily focus on the general trends in the 2PA changes rather than the absolute values.

Subsequently, the denser structures of SrTBAPy and BaTBAPy were also investigated to understand the drastic and unexpectedly large difference in their experimentally determined $\sigma^{(2)}$. However, here a different interplay of several factors was revealed. For SrTBAPy, the highest 2PA increase modulated by organic linkers is observed at the dimer, where the $TBAPy^{4-}$ units are stacked on top of each other ($\sigma^{(2)}$ is of 2.11 GM at 618 nm). Again, local excitonic interactions and intramolecular CT contribute to this excitation, as well as, in all other investigated dimers of SrTBAPy (Table S10, Supporting Information). However, the cumulative effect upon the consideration of larger assemblies, as in

NU-901, is missing (Figure 4c). Linkers are oriented differently as compared to NU-901 (nearly parallel versus zig-zag position) and the intermolecular distance between them is higher than in BaTBAPy (i.e., 6.86 Å for SrTBAPy, Figure S32, Supporting Information). Coupling between the molecules in the stacking direction drops down with the increase of intermolecular distance, thus limiting the CT impacting 2PA. This can be demonstrated by the distance screening calculations depicted in Figure S37: by decreasing the intermolecular distance by 2.45 Å, the $\sigma^{(2)}$ was increased by 1.5 GM.

Based on the reported polarization effect of the Sr metal in its SBU,[11f] we have calculated the 2PA change with the addition of the SBU (Table S6, Supporting Information). A significant increase of $\sigma^{(2)}$ up to 10.8 GM was revealed for the single linker molecule connected to the SBU. This change is caused by a difference in electron density delocalization through the linker with the density shift toward the SBU with an apparent (net) CT of 0.45% as indicated by the electron density differences visualized in Table S10c and Figure S38 (Supporting Information), and data calculated in Table S11 (Supporting Information). Thus, the polarization of the metal on the linker molecule and, in turn, the intramolecular CT of the molecule gets more long-distanced, which is known to enhance $\sigma^{(2)}$.[11e,f] Upon further investigation of packings, it is evident that this effect is getting quenched upon the aggregation of molecules in SrTBAPy: $\sigma^{(2)}$ is reduced to 7.05 and 5.14 GM at 670–690 nm in the stacked dimer with one and two SBUs, respectively. From the electron density differences visualized in Figure S38 (Supporting Information), significant changes in the electron hole occupation in a monomer and a dimer linked to the SBU are revealed. This indicates that the linker–metal CT characteristics are altered upon molecular assembly within the MOF: electronic delocalization is slightly changed and the apparent CT contribution is less pronounced in the dimer. It is 0.21% for the dimer connected to one SBU and lowers to 0.14% with the second SBU present (Table S11, Supporting Information). At the same time, the net CT between linkers in a dimer is rather low (0.10%), indicating inefficient electronic interaction between the SBU and the formed assembly. This can explain the unexpected decrease of $\sigma^{(2)}$ for SrTBAPy. (Note: The introduction of more metals leads to a redshift of the transitions, and transitions can be observed at higher wavelengths in accordance with the experiment).[19] In summary, the unexpectedly low activity of SrTBAPy can be attributed to the quenching of apparent CT contributions upon coordination with the SBUs, as well as to poor electronic coupling between neighboring chromophores and the SBU due to the spatial arrangement of the linkers.

From the crystal structure of BaTBAPy, we see that the assembled structure and the linker coordination of the SBU are different than for SrTBAPy (Figure 1; and Figure S32, Supporting Information). They allow the stacking of chromophores at a much closer distance of 3.41 Å (i.e., at nearly half the distance of 6.86 Å in SrTBAPy). BaTBAPy behaves similarly to NU-901, and the addition of chromophore linkers in the assembly, e.g., from Dimers to a Trimer, results in an increase of $\sigma^{(2)}$, e.g., from 3.96 to 7.56 GM at 730–740 nm between DimerE and a Trimer (Figure S36d, Supporting Information). This gets also evident from the analysis of the electron density differences upon excitation (Table S12, Supporting Information). The presence of intermolecular CT is evident in both assemblies of BaTBAPy, which was not observed in SrTBAPy. The apparent CT percentage reaches 0.92% for DimerE (Table S11, Supporting Information). Moreover, the CT during excitation to closely lying higher excited states in BaTBAPy is even more pronounced, further enhancing $\sigma^{(2)}$.

When comparing the intermolecular distances of the linkers in this MOF (see the distance screening in Figure S37, Supporting Information), a clear trend emerges: $\sigma^{(2)}$ decreases as the interchromophore distance increases. At the distance of 6.41 Å (similar to the observed distances between $TBAPy^{4-}$ in SrTBAPy), $\sigma^{(2)}$ is lowered by 3.1 GM, i.e., it can reach values of around 1 GM, showing a reduction of $\sigma^{(2)}$ of 78% as compared to the actual DimerE. Therefore, the smaller distance between chromophores in BaTBAPy enhances chromophore intermolecular interactions, partially helping to explain the experimentally observed enhancement of $\sigma^{(2)}$ in BaTBAPy as compared to SrTBAPy. To our surprise, the interaction energy of the dimer extracted from BaTBAPy is 204.1 kJ mol^{-1}, indicating strong coupling between the chromophores. The interaction energy decreases (to 172 kJ mol^{-1}) in the case of a very similar dimer, i.e., DimerA (comparison in Figures S39 and S40, Supporting Information). This effect is related to the subtle differences in the overlap of frontier orbitals. Furthermore, a polarization effect associated with the SBU in BaTBAPy is evident (Figures S36d and S38, Supporting Information). However, it differs from the polarization seen in SrTBAPy discussed previously. First, there is no significant enhancement of 2PA for the chromophore calculated with one SBU unit (see the spectrum depicted with blue dashed line in Figure S36d, Supporting Information). The effect increases when a linker forms an ionic-like type bonding with the Ba atom (see the spectrum marked with blue solid line in Figure S36d, Supporting Information), i.e., $\sigma^{(2)}$ may increase to 11 GM. However, when considering larger assemblies (e.g., a dimer with one and two SBUs attached), the $\sigma^{(2)}$ increases to 13.8 and 29.6 GM, respectively (Figure 4d). This effect is assumed to be linked to changes in electron density delocalization and induced changes in CT between linkers in a dimer, as well as the electron density shift between the linker and the SBU (**Figure 5**). A contribution from the electron density localized on the phenyl ring directly attached to the SBU is visible in Figure S38. The apparent CT between linkers in DimerA, linked to two SBUs, is 2.23%, while the CT contribution via direct interaction with the SBU (i.e., linker-metal CT) is a maximum of 0.18% (Table S11, Supporting Information).

The shift in electron density upon 2PA excitation of the dimer, which is connected to two SBUs, is shown in Figure 5a. The electron donating regions from where electron density moves upon the excitation is marked in blue, while the electron accepting region is in green. In the dimer, the frontier orbitals involved in this transition (Figure 5b) exhibit a delocalized nature (for example, holes are distributed to 37.37% and 62.63% on both linkers, see Tables S11 and S12, Supporting Information) and the excitation demonstrates a mixed local exciton and CT character. In the presence of SBUs, orbital delocalization changes significantly with a higher hole localization on the linker part that is in close contact with the metal (regions in blue in Figure 5a). Thus, holes attain a 98.30 – 1.53% distribution. This electron density moves to the other part of the molecule when excitation occurs, i.e., from the HOMO to the LUMO+1 orbital. This increase in CT distance reflects a reduced local exciton character of the excitation,

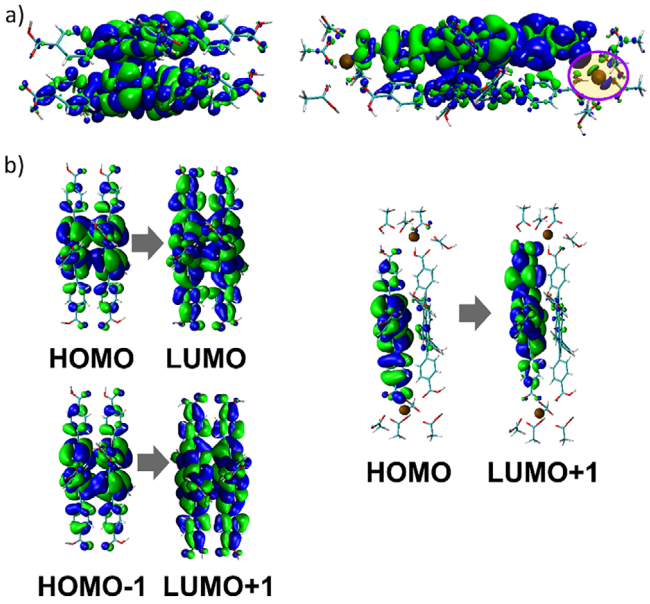

Figure 5. Electron density difference between the first excitation and the ground state a) and transition orbitals b) in the dimer extracted from BaTBAPy, with and without the Ba-based SBU. Upper panel: Electron-donating regions, from which electron density moves upon excitation, are marked in blue, while electron-accepting regions are in green. The change in CT characteristics in DimerE is shown in Figure S39, Supporting Information.

further altering the CT properties and charge separation. As a result, the net CT is enhanced, leading to an increased 2PA cross section. Moreover, the orbital overlap between the molecules in the dimer linked to SBUs is different, demonstrating a strong impact of the SBU on the communication in the dimer assembly.

Based on these observations, we propose that the increase in 2PA for BaTBAPy arises from stacking induced interactions (enabling coupling between chromophores) and linker–SBU coordination. These factors alter electron delocalization within the assembly, facilitating apparent CT both between the linker and the metal node (0.18%) and between assembled molecules (2.23%). Notably, the CT contribution from the molecular assembly is estimated to be more than an order of magnitude stronger. We believe that this complementary and cumulative effect causes a considerable change in the 2PA response, consistent with the experimental observation. Therefore, the 2PA increase in this MOF tends to be directed by the MOF topology and chromophore packing, as well as the polarization effects induced by the SBU, further tuning the 2PA.

When comparing the 2PA spectra measured experimentally with those calculated using TD-DFT, we observed the presence of low-energy peaks for BaTBAPy at wavelengths below 850 nm (Figure 3b). We found that these peaks may arise from subtle differences in the local environment of the SBU and slight variations in the coordination shell, which impact the local electronic nature of the metal. Similar peaks were detected for DimerE (Figure S40, Supporting Information), originating from the contributions of transition orbitals occupying small neutralizing substituents coordinated to Ba, used to represent the metal's coordination shell. This suggests that the peaks observed in Figure 3 may be associated with subtle deviations in the SBU coordination within the material.

3. Conclusion

In conclusion, the synthesis of the linker H_4TBAPy and its four corresponding MOFs (NU-1000, NU-901, SrTBAPy, and BaTBAPy) have been presented. After structural characterization the MOFs have been analyzed for their 1PA and 2PA properties, where H_4TBAPy showed topology-dependent activity variations in the different MOFs. The order of $\sigma^{(2)}$ was revealed to be SrTBAPy < NU-1000 < NU-901 < BaTBAPy with the respective highest $\sigma^{(2)}$ of 2.1×10^3, 1.2×10^4, 1.8×10^4, and 8.2×10^4 GM. Surprisingly, SrTBAPy is showing the lowest activity compared to the others despite closer packed ligands (as compared to NU-1000 and NU-901) and the previously confirmed polarization effect induced by the Sr-SBU (as compared to BaTBAPy).

DFT and TD-DFT calculations were performed to investigate the reason for the differing $\sigma^{(2)}$ of the MOFs. Calculations on assemblies extracted from the MOF crystal structures revealed a topology-dependent enhancement of 2PA activity. This enhancement arises from subtle variations in CT characteristics and electronic density delocalization, driven by changes in linker orientation and intermolecular coupling. In SrTBAPy, the CT between linkers is hindered by inefficient coupling between the linkers with a distance of 6.41 Å. However, in the polymorphic structures of NU-1000 and NU-901, the continuous anisotropic CT pathway in NU-901 results in a slightly higher 2PA compared to NU-1000, surpassing the $\sigma^{(2)}$ of SrTBAPy by a factor of 8.4. The increase of the 2PA as a function of the linker orientation in the polymorphs was revealed, and the influence of the exciton confinement in the smaller triangular pore of NU-1000, which is disabling the continuous enhancement of its 2PA was uncovered. In BaTBAPy, the closer packing of chromophores and shorter intermolecular distances enable strong intermolecular interactions and high electron density delocalization. These characteristics are modified significantly upon coordination to the metal node, facilitating efficient electronic coupling and pronounced polarization effects induced by the metal center. This triggers the increase of the apparent intermolecular CT as well as the CT contributions between the linker and the SBU, which is strongly enhancing 2PA. This electronic effect of the SBU was observed to be topology-dependent when comparing SrTBAPy and BaTBAPy. For SrTBAPy, no synergistic enhancement between linker and metal polarization was observed. In contrast, BaTBAPy exhibits clear evidence of such a synergistic interaction, consistent with experimental results showing BaTBAPy having the highest and SrTBAPy the lowest $\sigma^{(2)}$.

The findings highlight the complex nature of $\sigma^{(2)}$ enhancement in MOFs, driven by structural parameters, electronic interactions, SBU contributions, and their interplay. This underscores the importance of understanding structure–property relationships in the MPA of MOFs. The results shown advance the understanding of MPA in hybrid materials and MOFs, providing a foundation for materials design principles. Future studies can further explore the delicate balance between topology, metal coordination, and chromophore arrangement to achieve targeted optical properties.

4. Experimental Section

Materials and Methods: All purchased reagents were received from chemical suppliers and used without further purification, if not stated otherwise. All reactions with air- and moisture-sensitive compounds were carried out under standard Schlenk techniques using Argon 4.6 (*Westfalen*) or in a glovebox (UNIlab, M. Braun). The required glassware was flame-dried in a vacuum before use. Elemental analysis was performed at the Elemental Analysis Lab of the CRC at the Technical University of Munich. Analysis of C, H, and N values was conducted using the flash combustion method at 1800 °C. NMR spectra were recorded on a Bruker AV400 at room temperature at 400 MHz. PXRD measurements were recorded on a *Rigaku* Miniflex diffractometer equipped with Cu radiation (λ = 1.54 Å), and a D/teX Ultra high-speed 1D silicon strip detector. An Edinburgh FS5 fluorescence spectrometer equipped with a 150 W Continuous Wave Xenon Lamp source for excitation was used to acquire steady-state emission spectra. Emission measurements on solid samples were collected on PMMA films of the desired materials using the front-facing module. IR measurements were conducted on a *PerkinElmer* Frontier FT-IR spectrometer. Broadband two-photon excitation spectra of linker molecules and CPs were recorded using a home-built setup based on the noncollinear optical parametric amplifier and a common-path birefringent interferometer.[11g] A TGA/STA 409 PC apparatus from *Mettler-Toledo Intl. Inc*. was used for thermogravimetric analysis under synthetic air with a continuous heating ramp of 10 °C min^{-1}. Electron diffraction measurements for BaTBAPy were collected using the *Rigaku* XtaLAB Synergy-ED, equipped with a *Rigaku* HyPix-ED detector optimized for operation in the continuous rotation 3D-ED experimental setup.[20] Data acquisition was performed at 170 K under high vacuum with an electron wavelength of 0.0251 Å (200 kV). The instrument was operated, and the diffraction data were processed in the program CrysAlis^{Pro}.[21] A multiscan absorption correction was performed using spherical harmonics implemented in SCALE3 ABSPACK scaling algorithm in CrysAlis^{Pro}. The structure was solved using ShelXT, and subsequently, refined with kinematical approximation using ShelXL in the crystallographic program suite Olex2.[22] All diffuse reflectance spectra were recorded on a *Shimadzu* UV-3600 Plus UV−vis−NIR spectrophotometer with an ISR-603 integrating sphere attachment. Powder samples were fixed between two quartz glass slides for measurement. For the measurement, the following parameters were used: medium scan speed, slit width (20) with external (3Detector) unit, enabled stair correction, baseline correction (BaSO4 background), S/R exchange normal, and slit and detector lock normal. The fluorescence QY was measured with the absolute photoluminescence QY measurement system C11347-12 Quantaurus by *Hamamatsu*. The linker was measured in solution in quartz glass cuvettes and the MOF samples as thin film in PMMA in a quartz glass laboratory dish. After referencing the empty cuvettes and laboratory dishes the QY was determined by the scan method in a wavelength range of 280–420 nm with a step size of 5 nm for all samples and averaging the single measurement points to get the QY of each sample additionally using a reabsorption correction. UV−vis spectra in solution were recorded on a double-beam Lambda 365 UV−Vis spectrophotometer from PerkinElmer.

Synthesis: *1,3,6,8-tetrakis(4-(ethoxycarbonylphenyl)pyrene) (Et_4TBAPy)* The synthesis of Et_4TBAPy was performed using a modified literature synthesis.[12] Tetrabromopyrene (2.85 g, 5.50 mmol, 1.0 equiv.) is refluxed with 4-ethoxycarbonylphenylboronic acid (6.00 g, 30.9 mmol, 6.0 equiv.), basic potassium phosphate (5.00 g, 23.6 mmol, 4.0 equiv.), and tetrakis(triphenylphosphine)palladium (0) (0.10 g, 0.1 mmol, 0.02 equiv.) in degassed and dried dioxane (50 mL) under argon atmosphere for 3 days. After cooling to room temperature, 130 mL water was added, and the precipitate was filtrated. The filtrate was washed with 60 mL of water and 130 mL of acetone. Subsequently, the product was resolved in hot $CHCl_3$ and, after cooling down, precipitated with MeOH. The bright yellow suspension was filtered and dried in an oven to give 2.35 g (2.96 mmol, 54%) of a bright yellow powder of Et_4TBAPy.

^{1}H-NMR (400 MHz, $CDCl_3$): δ (ppm) = 8.27–8.21 (m, 8H), 8.15 (s, 4H), 8.01 (s, 2H), 7.78–7.71 (m, 8H), 4.46 (q, J = 7.1 Hz, 8H), 1.45 (t, J = 7.1 Hz, 12H)

1,3,6,8-tetrakis(benzoic acid)pyrene (H_4TBAPy) The synthesis of H_4TBAPy was performed using a modified literature synthesis.[12] 2.35 g of Et_4TBAPy (2.96 mmol, 1.0 equiv.) were solved in a 500 mL flask in 250 mL dioxane. Afterward, 3.65 g KOH (65.1 mmol, 22.0 equiv.) solved in 200 mL water are added and refluxed for 18 h. After completion of the reaction time, the solvent was removed on a rotary evaporator, and the residue was solved in water to give a bright yellow solution. Following this, HCl was added, and a yellow precipitate forms. This precipitate was centrifuged and dried under vacuum to give 1.85 g of H_4TBAPy (2.71 mmol, 92%).

^{1}H-NMR: (400 MHz, DMSO-d_6) δ (ppm) = 13.12 (s, 4H), 8.21–8.13 (m, 12H), 8.06 (s, 2H), 7.87–7.80 (m, 8H).

NU-1000 The synthesis of NU-1000 was performed using a modified literature synthesis.[13a] Zirconyl chloride octahydrate (0.39 g, 1.20 mmol, 1.0 equiv.) and biphenyl-4-carboxylic acid (17.6 g, 88.4 mmol, 74.0 equiv.) were dissolved in 32 mL of DMF in a 100 mL glass vial and heated to 100 °C for 1 h in an oven. Additionally, H_4TBAPy (50.0 mg, 0.07 mmol) was dissolved in 3 mL of DMF in a 20 mL scintillation vial. The two hot solutions were mixed, and the reaction was held at 100 °C for 24 h in an oven. The bright yellow product was isolated via centrifugation and washed with DMF (3 × 25 mL) and acetone (3 × 25 mL) (yield = 52 mg). The yellow powder was further suspended in 12 mL DMF, and 0.5 mL of 8 M aqueous HCl was added. The suspension was heated in an oven at 100 °C for 18 h. After cooling to room temperature, the powder was isolated by centrifugation and washed with DMF (3 × 25 mL) and acetone (3 × 25 mL) to yield 50 mg of NU-1000 after drying.

NU-901 The synthesis of NU-901 was performed using a modified literature synthesis.[13b] 97 mg $Zr(acac)_2$ (0.2 mmol, 3.33 equiv.) and 3.02 g 4-aminobenzoic acid (22 mmol, 367 equiv.) were mixed in 8 mL DMF in a 20 mL scintillation vial and heated to 100 °C. Simultaneously a solution of 40 mg H_4TBAPy (0.06 mmol, 1.00 equiv.) in 2 mL DMF was prepared and heated to 100 °C and subsequently given to the node solution. This solution was held at 100 °C for another 18 h. Following this, the yellow participants were isolated by centrifugation and washed with DMF (3 × 25 mL) and acetone (3 × 25 mL). After drying the obtained powder was suspended in 12 mL DMF and 0.5 mL of 8 M aqueous HCl and heated in an oven at 100 °C for 18 h. The obtained yellow participant was isolated by centrifugation and washed with DMF (3 × 25 mL) and acetone (3 × 25 mL), yielding 32 mg of NU-901 after drying.

[Sr_2TBAPy$(H_2O)_2$(DMF)] × $(H_2O)_{1.8}$ × $(DMF)_{4.7}$ (SrTBAPy) The synthesis of SrTBAPy was performed using a modified literature synthesis.[14] 7.50 mg of $Sr(NO_3)_2$ (0.04 mmol, 4.84 equiv.) were weighed in a 4 mL scintillation vial. Subsequently, 0.5 mL H2O, 5.00 mg of H_4TBAPy (73.2 µmol, 1.00 equiv.) was solved in 2.5 mL DMF, and 10 µL HCl was added. This suspension was heated at 85 °C for 3 days, filtered off, and washed with DMF. After drying, 4.51 mg of yellow crystalline SrTBAPy was obtained.

[Ba_2TBAPy$(DMF)_2$] × $(H_2O)_2$ (BaTBAPy) In a 4 mL scintillation vial 9.26 mg $Ba(NO_3)_2$ (0.04 mmol, 4.84 equiv.) were mixed with 0.5 mL H_2O, 5.00 mg H_4TBAPy (73.2 µmol, 1.00 equiv.) solved in 2.5 mL DMF and 10 µL HCl. This suspension was put into an oven for 3 days at 85 °C. The obtained yellow solid 3.92 mg BaTBAPy was filtered and washed with DMF.

Elemental Analysis: calcd. for $C_{50}H_{40}Ba_2N_2O_{12}$: C, 52.89; H, 3.55; Ba, 24.19; N, 2.47; O 16.91. meas. C, 52.51; H, 3.10; N; 2.48.

Computational Details: The ground and excited state properties of the H_4TBAPy linker and assembly clusters (i.e., dimers and trimers positioned in distinct orientations, see Table S5, Supporting Information) extracted from the crystal structures of the MOFs were examined through the DFT and the TD-DFT approaches using Turbomole V7.6.[23] The resolution-of-identity (RI) approximation was applied during the calculation. Only the monomer structures were fully optimized using DFT both in the gas phase and in *implicit* DMF solvent. The solvation model COSMO (COnductor-like Screening MOdel) was used with a refractive index of 1.43 and a dielectric constant of 36.7, corresponding to DMF.[24] Vibrational analysis confirmed that a true minimum was reached after optimization. All calculations were performed using the long-range corrected hybrid CAM-B3LYP functional with def2-SVP (split-valence polarized) basis set.[25] The D3 dispersion correction with Becke–Johnson damping (D3BJ) was applied to account for van der Waals interactions.[26] The energy convergence

threshold for the geometry optimization of monomers was set to 1×10^{-8} Hartree.

The extracted linker assemblies were considered with the single point calculation and energy convergence threshold set to 1×10^{-7} Hartree. SBUs were excluded in the computation of NU-1000 and NU-901 due to the computational cost and the similarity of the SBU in both cases. Considering the previously reported results indicating the SBU influence in the case of Sr- and Ba-based SBUs, the calculation was performed with and without SBUs.[11f] The systems calculated and the representation of the SBU are given in Table S6 (Supporting Information). Effective core potentials (def-ecp) were applied for the Ba and Sr atoms. The interaction energy of the monomers in a dimer was calculated as the difference between the total energy of the extracted dimer and the single-point energies of the respective monomers that make up the dimer. Using the same setup as explained above, 1PA and 2PA spectra were calculated considering ten singlet vertical excitations.[27] Linker assemblies were calculated in the gas phase, while monomer spectra were calculated in the gas phase and *implicit* DMF for comparison. The spectra of linker monomers were calculated starting from their respective optimized ground state geometry. In specific cases, e.g., for the estimation of the SBU effect, the single point extracted from the crystal structure was considered. Spectra were plotted using half width at half maximum (HWHM) of 0.1 eV and Lorentzian type broadening function. 2PA spectra were calculated considering a single, linearly polarized laser beam. Changes in electron density upon excitation were calculated using Turbomole and visualized using Visual Molecular Dynamics (VMD) applying 0.02 a.u. isovalue for individual orbitals and 0.0002 a.u. for the electron density difference. The quantification of the charge transfer was performed using Inter-Fragment Charge Transfer analysis using Multiwfn (version 3.8).[28]

[CCDC 2 420 113 contains the supplementary crystallographic data for this paper. These data can be obtained free of charge from The Cambridge Crystallographic Data Centre via www.ccdc.cam.ac.uk/data_request/cif.]

Supporting Information

Supporting Information is available from the Wiley Online Library or from the author.

Acknowledgements

This research was funded by the Deutsche Forschungsgemeinschaft (DFG) via SPP 1928 COORNETs, GRK 2450 "Scale bridging methods of computational nanoscience" and within the frame of the EXC 2089 Cluster of Excellence. J.H. and H.H. acknowledged funding by the DFG, Project Nos. 548646502, SPP1928 and EXC2089. The authors acknowledged support by the state of Baden–Württemberg through bwHPC and the DFG through Grant No. INST 40/575-1 FUGG (JUSTUS 2 cluster) under project bw20F004. Financed by the Ministry of Science, Research and the Arts of Baden–Württemberg as part of the sustainability financing of the projects of the Excellence Initiative II. The TUM is greatly acknowledged for its institutional funding. S.N.D. thanked the TUM Graduate School for financial support and F. Haska for help with the experiments. H.P.H. acknowledged funding by the Deutscher Akademischer Austauschdienst (DAAD). H.H. acknowledged support from Chinese Scholarship Council (CSC No. 202106870026).

Open access funding enabled and organized by Projekt DEAL.

Conflict of Interest

The authors declare no conflict of interest.

Data Availability Statement

The data that support the findings of this study are available in the Supporting Information of this article.

Keywords

metal–organic frameworks, multiphoton absorption, nonlinear optics, structure–property relationships

Received: March 14, 2025
Revised: May 31, 2025
Published online:

[1] G. I. Stegeman, R. A. Stegeman, *Nonlinear Optics: Phenomena, Materials and Devices*, Wiley, Hoboken, NJ **2012**.
[2] a) G. S. He, L.-S. Tan, Q. Zheng, P. N. Prasad, *Chem. Rev.* **2008**, *108*, 1245; b) V. Nathan, A. H. Guenther, S. S. Mitra, *J. Opt. Soc. Am. B* **1985**, *2*, 294.
[3] D. R. Miller, J. W. Jarrett, A. M. Hassan, A. K. Dunn, *Curr. Opin. Biomed. Eng.* **2017**, *4*, 32.
[4] J. D. Bhawalkar, N. D. Kumar, C.-F. Zhao, P. N. Prasad, *J. Clin. Laser Med. Surg.* **1997**, *15*, 201.
[5] S. Maruo, O. Nakamura, S. Kawata, *Opt. Lett.* **1997**, *22*, 132.
[6] L. W. Tutt, T. F. Boggess, *Prog. Quantum Electron.* **1993**, *17*, 299.
[7] a) J. Bhawalkar, G. He, P. Prasad, *Rep. Prog. Phys.* **1996**, *59*, 1041; b) F. Zhou, X. Ran, D. Fan, S. Lu, W. Ji, *Adv. Opt. Mater.* **2021**, *9*, 2100292; c) Y. Wang, V. D. Ta, Y. Gao, T. C. He, R. Chen, E. Mutlugun, H. V. Demir, H. D. Sun, *Adv. Mater.* **2014**, *26*, 2954.
[8] a) R. Medishetty, J. K. Zaręba, D. Mayer, M. Samoć, R. A. Fischer, *Chem. Soc. Rev.* **2017**, *46*, 4976; b) S. J. Weishäupl, D. C. Mayer, Y. Cui, P. Kumar, H. Oberhofer, R. A. Fischer, J. Hauer, A. Pöthig, *J. Mater. Chem. C* **2022**, *10*, 6912.
[9] a) D. C. Mayer, A. Manzi, R. Medishetty, B. Winkler, C. Schneider, G. Kieslich, A. Pöthig, J. Feldmann, R. A. Fischer, *J. Am. Chem. Soc.* **2019**, *141*, 11594; b) N. B. Shustova, B. D. McCarthy, M. Dinca, *J. Am. Chem. Soc.* **2011**, *133*, 20126; c) R. Haldar, M. Jakoby, M. Kozlowska, M. Rahman Khan, H. Chen, Y. Pramudya, B. S. Richards, L. Heinke, W. Wenzel, F. Odobel, *Chem. – Eur. J.* **2020**, *26*, 17016.
[10] A. Kirchon, L. Feng, H. F. Drake, E. A. Joseph, H.-C. Zhou, *Chem. Soc. Rev.* **2018**, *47*, 8611.
[11] a) N. Liu, Z. Chen, W. Fan, J. Su, T. Lin, S. Xiao, J. Meng, J. He, J. J. Vittal, J. Jiang, *Angew. Chem., Int. Ed.* **2022**, *134*, 202115205; b) H. S. Quah, W. Chen, M. K. Schreyer, H. Yang, M. W. Wong, W. Ji, J. J. Vittal, *Nat. Commun.* **2015**, *6*, 7954; c) B. B. Rath, D. Kottilil, W. Ji, J. J. Vittal, *ACS Appl. Mater. Interfaces* **2023**, *15*, 26939; d) R. Medishetty, V. Nalla, L. Nemec, S. Henke, D. Mayer, H. Sun, K. Reuter, R. A. Fischer, *Adv. Mater.* **2017**, *29*, 1605637; e) R. Medishetty, L. Nemec, V. Nalla, S. Henke, M. Samoć, K. Reuter, R. A. Fischer, *Angew. Chem., Int. Ed.* **2017**, *56*, 14743; f) S. J. Weishäupl, Y. Cui, S. N. Deger, H. Syed, A. Ovsianikov, J. Hauer, A. Pöthig, R. A. Fischer, *Chem. Mater.* **2022**, *34*, 7402; g) S. N. Deger, Y. Cui, J. Warnan, R. A. Fischer, F. Šanda, J. Hauer, A. Pöthig, *ACS Appl. Opt. Mater.* **2024**, *2*, 1770; h) H. S. Quah, V. Nalla, K. Zheng, C. A. Lee, X. Liu, J. J. Vittal, *Chem. Mater.* **2017**, *29*, 7424; i) H. Yuan, X. Xu, Z. Qiao, D. Kottilil, D. Shi, W. Fan, Y. D. Yuan, X. Yu, A. Babusenan, M. Zhang, W. Ji, *Adv. Opt. Mater.* **2024**, *12*, 2302405; j) D. C. Mayer, J. K. Zaręba, G. Raudaschl-Sieber, A. Pöthig, M. Chołuj, R. Zaleśny, M. Samoć, R. A. Fischer, *Chem. Mater.* **2020**, *32*, 5682; k) S.-C. Wang, Q.-S. Zhang, Z. Wang, L. Zheng, X.-D. Zhang, Y.-N. Fan, P.-Y. Fu, X.-H. Xiong, M. Pan, *Angew. Chem., Int. Ed.* **2022**, *61*, 202211356; l) S. N. Deger, A. Mauri, Y. Cui, S. J. Weishäupl, A. D. Özdemir, H. Syed, A. Ovsianikov, W. Wenzel, A. Pöthig, J. Hauer, M. Kozlowska, R. A. Fischer, *Adv. Funct. Mater.* **2025**, 2424656.
[12] T. C. Wang, N. A. Vermeulen, I. S. Kim, A. B. F. Martinson, J. F. Stoddart, J. T. Hupp, O. K. Farha, *Nat. Protoc.* **2016**, *11*, 149.
[13] a) T. E. Webber, W.-G. Liu, S. P. Desai, C. C. Lu, D. G. Truhlar, R. L. Penn, *ACS Appl. Mater. Interfaces* **2017**, *9*, 39342; b) S. J. Garibay,

I. Iordanov, T. Islamoglu, J. B. DeCoste, O. K. Farha, *CrystEngComm* **2018**, *20*, 7066.
[14] S. Sudan, A. Gładysiak, B. Valizadeh, J.-H. Lee, K. C. Stylianou, *Inorg. Chem.* **2020**, *59*, 9029.
[15] Y.-R. Meng, M.-J. Xu, S.-F. Li, B.-C. Li, G. Zhang, J. Su, *Inorg. Chem.* **2024**, *63*, 17856.
[16] K. Muralirajan, I. S. Khan, L. Garzon-Tovar, R. Kancherla, N. Kolobov, A. Dikhtiarenko, M. Almalki, A. Shkurenko, A. Rendón-Patiño, V. Guillerm, K. N. Le, G. Shterk, H. Zhang, C. H. Hendon, M. Eddaoudi, J. Gascon, M. Rueping, *Adv. Mater.* **2024**, *37*, 2405646.
[17] N. S. Makarov, M. Drobizhev, A. Rebane, *Opt. Express* **2008**, *16*, 4029.
[18] a) D.-G. Ha, R. Wan, C. A. Kim, T.-A. Lin, L. Yang, T. Van Voorhis, M. A. Baldo, M. Dincă, *Nat. Mater.* **2022**, *21*, 1275; b) S. S. Rajasree, J. Yu, S. M. Pratik, X. Li, R. Wang, A. S. Kumbhar, S. Goswami, C. J. Cramer, P. Deria, *J. Am. Chem. Soc.* **2022**, *144*, 1396.
[19] P. Deria, J. Yu, T. Smith, R. P. Balaraman, *J. Am. Chem. Soc.* **2017**, *139*, 5973.
[20] a) S. Ito, F. J. White, E. Okunishi, Y. Aoyama, A. Yamano, H. Sato, J. D. Ferrara, M. Jasnowski, M. Meyer, *CrystEngComm* **2021**, *23*, 8622; b) K.-N. Truong, S. Ito, J. M. Wojciechowski, C. R. Göb, C. J. Schürmann, A. Yamano, M. Del Campo, E. Okunishi, Y. Aoyama, T. Mihira, N. Hosogi, J. Benet-Buchholz, E. C. Escudero-Adán, F. J. White, J. D. Ferrara, R. Bücker, *Symmetry* **2023**, *15*, 1555.
[21] *Rigaku Oxford Diffraction, CrysAlisPro Software System*, Rigaku Corporation, Wrocław, Poland **2025**, (version 1.171.44.91a).
[22] a) G. M. Sheldrick, *Acta Cryst.* **2015**, *A71*, 3; b) G. M. Sheldrick, *Acta Cryst.* **2015**, *C71*, 3; c) Rigaku Oxford Diffraction, *AutoChem 7 Software System in Conjunction with OLEX2*, Rigaku Corporation, Wrocław, Poland **2025**, (version 1.5-ac7-013); d) O. V. Dolomanov, L. J. Bourhis, R. J. Gildea, J. A. K. Howard, H. Puschmann, *J. Appl. Cryst.* **2009**, *42*, 339.
[23] S. G. Balasubramani, G. P. Chen, S. Coriani, M. Diedenhofen, M. S. Frank, Y. J. Franzke, F. Furche, R. Grotjahn, M. E. Harding, C. Hättig, A. Hellweg, B. Helmich-Paris, C. Holzer, U. Huniar, M. Kaupp, A. Marefat Khah, S. Karbalaei Khani, T. Müller, F. Mack, B. D. Nguyen, S. M. Parker, E. Perlt, D. Rappoport, K. Reiter, S. Roy, M. Rückert, G. Schmitz, M. Sierka, E. Tapavicza, D. P. Tew, et al., *J. Chem. Phys.* **2020**, *152*, 184107.
[24] A. Klamt, G. Schüürmann, *J. Chem. Soc., Perkin Trans. 2* **1993**, *799*, 799.
[25] a) T. Yanai, D. P. Tew, N. C. Handy, *Chem. Phys. Lett.* **2004**, *393*, 51; b) F. Weigend, R. Ahlrichs, *Phys. Chem. Chem. Phys.* **2005**, *7*, 3297.
[26] S. Grimme, S. Ehrlich, L. Goerigk, *J. Comput. Chem.* **2011**, *32*, 1456.
[27] D. H. Friese, C. Hättig, K. Ruud, *Phys. Chem. Chem. Phys.* **2012**, *14*, 1175.
[28] T. Lu, F. Chen, *J. Comput. Chem.* **2012**, *33*, 580.